Fingerprinting ore processes in orogenic auriferous systems: Insights into metallogenic and exploration implications from argillite-hosted iron sulphide nodules from the Timmins-Matheson gold corridor

Jean-Luc Pilote[1]*, Simon E. Jackson[2], Patrick Mercier-Langevin[1], Benoît Dubé[1], Christopher J.M. Lawley[2], Duane C. Petts[2], Zhaoping Yang[2], Ed van Hees[3], and Dave Rhys[4]

[1]Geological Survey of Canada, 490 rue de la Couronne, Québec, Quebec G1K 9A9
[2]Geological Survey of Canada, 601 Booth Street, Ottawa, Ontario K1A 0E8
[3]Ontario Geological Survey, 5520 Hwy 101 East, South Porcupine, Ontario, Canada P0N 1H0
[4]Panterra Geoservices Inc., 14180 Greencrest Drive, Surrey, British Columbia, Canada V4P 1L9
*Corresponding author's e-mail: jean-luc.pilote@canada.ca

ABSTRACT

Orogenic Au deposits of the world-class Timmins-Porcupine Au camp in Abitibi and its surroundings are commonly hosted by carbonaceous to non-carbonaceous argillite sequences, which contain Au-rich ($\leq$10 ppm Au) nodules and concretions; two features widely considered to be diagenetic, but can be equivocal in some highly strained and hydrothermally altered zones. Hence, the goals of this research activity are to (1) fingerprint pyrite of diagenetic or epigenetic origin, (2) constrain factors that control Au uptake in diagenetic pyrite, and (3) determine if early Au enrichment fundamentally influences overprinting orogenic Au mineralization. Pyrite nodules and concretions are generally composed of two textural domains: a core and a rim. The pyrite rims exhibit much more textural complexity than the pyrite cores. Multivariate analysis of trace element data derived from laser ablation-inductively coupled plasma-mass spectrometry reveal a clear geochemical distinction between epigenetic textures (granoblasts, porphyroblasts, idiomorphic overgrowths) and nodules/concretions. In the Timmins-Matheson region, disparate pyrite textures can be discriminated simply by the abundance of thallium. Nodules and concretions also show geochemical attributes that are inherited from the composition of the rock assemblage in which they form. Regardless of their host rocks, the core and rim of the nodules possess different but systematic geochemical signatures, which were constrained with the help of multivariate statistics; Ni, As, Se, Ag, Sb, Au, Pb, and Bi tend to concentrate into the core, whereas Mo and Tl ($\pm$Mn) tend to concentrate into the rim. In situ Fe isotope analyses of three pyrite nodules reveal intra-grain variations in δ^{56}Fe values that range from -3.11 to 0.74‰, with 30% of the values <-2.5‰, which has, in the literature to date, been recorded only in Archean diagenetic pyrite in black shale. The results contribute to a framework that helps improving our interpretation of the genesis of pyrite nodules in deformed and metamorphosed sedimentary rocks, which will ultimately minimize uncertainties related to the interpretation of ore-forming processes.

INTRODUCTION

The Timmins-Matheson corridor of the Archean southern Abitibi greenstone belt encompasses one of the highest concentrations of Au deposits globally, with the Timmins-Porcupine camp alone having produced over 75 Moz (2125 metric tonnes) Au (Dubé et al., 2017). This ~60 km long, east-west-oriented corridor is characterized by volcanic and sedimentary assemblages that are host to numerous greenstone-hosted quartz-carbonate (orogenic) Au deposits, and is transected by the regional Destor-Porcupine and Pipestone fault zones (Fig. 1). Sulphide-bearing carbonaceous sedimentary units within the Timmins-Matheson area are common, although volumetrically a minor part of the sedimentary sequence, and many are spatially associated with orogenic Au deposits (Hannington et al., 2012; Dubé et al., 2017). Moreover, volcanogenic massive sulphide (VMS) and komatiite-hosted Ni-Cu-(PGE) deposits are also known to be hosted by, or closely associated with, such sedimentary units (Hannington et al., 1999; Mercier-Langevin et al., 2007; Houlé et al., 2010; Pilote et al., 2020). Common to these sedimentary rocks are sulphides that occur as individual or clusters of pyrite nodules (e.g. Jonasson et al., 1999; Gray and Hutchinson, 2001; Hannington et al., 2012).
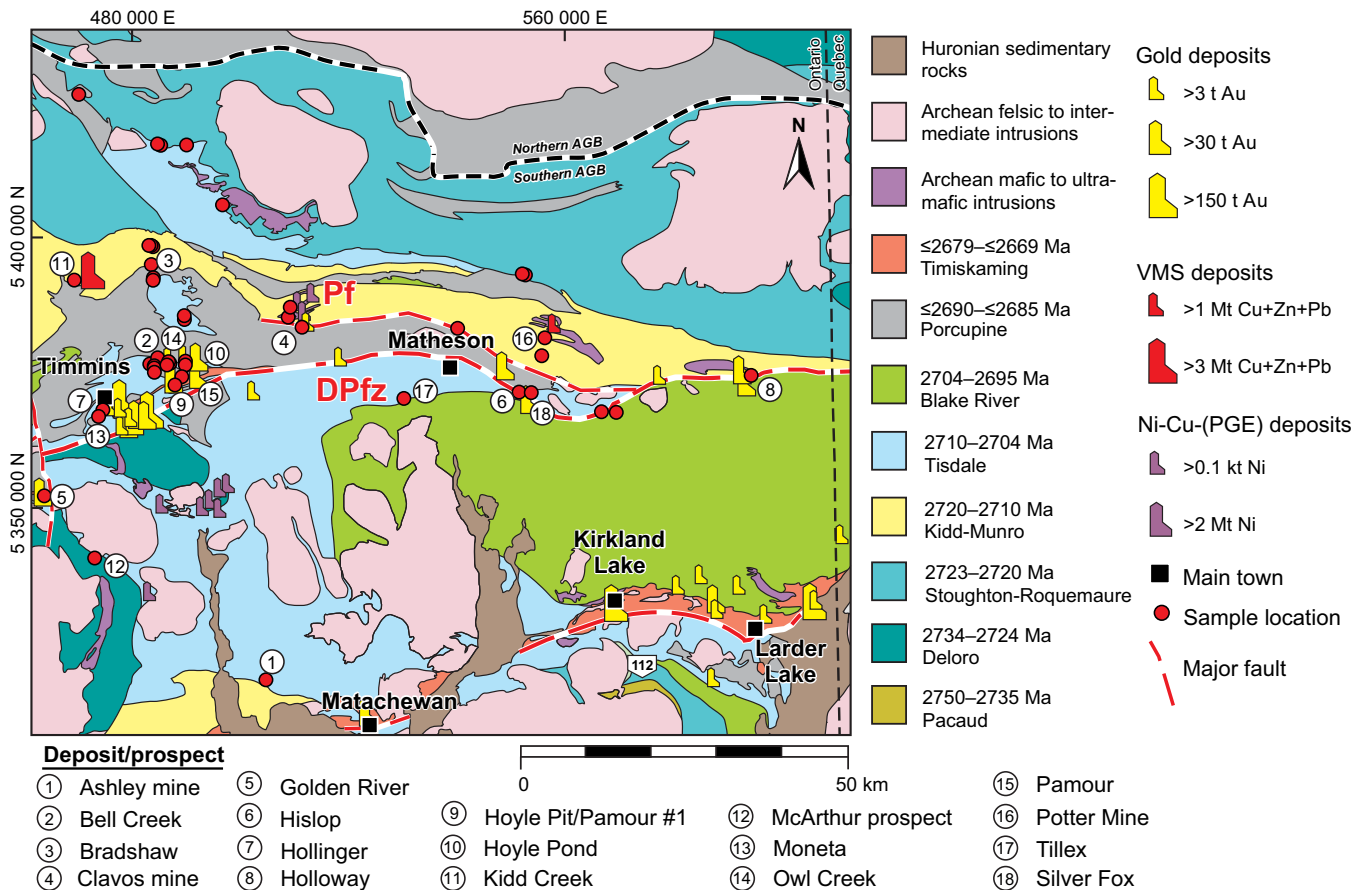
Figure 1. Simplified geological map of the western portion of the southern Abitibi greenstone belt (AGB) and location of samples collected (red circle). Map after Dubé et al. (2017). Abbreviations: DPfz = Destor-Porcupine fault zone, Pf = Pipestone fault.

Early work reported Au values in pyrite nodules ranging from a few ppb to >10 ppm Au (Jackson et al., 2017; Pilote et al., 2019), with the core typically enriched relative to its rim (Pilote et al., 2019). The factors controlling this enrichment are not fully understood. Pyrite nodules are widely accepted to be authigenic and diagenetic (e.g. Bonnell and Anderson, 1987; Guy et al., 2010, 2014; Rickard, 2012; Gregory et al., 2019). However, in high-strain zones and/or hydrothermally overprinted areas, their genesis is equivocal. For example, some could arguably be round, S-reactive lithic clasts, such as carbonaceous and/or Fe-rich argillite, that underwent partial or complete replacement by pyrite (i.e. hydrothermal pseudomorphs) resulting in a spherical or elliptical shape that could be misidentified as diagenetic (similar to what some have argued for the origin of rounded pyrite in the Witwatersrand basin: Barnicoat et al., 1997; Phillips and Law, 2000). The distinction between diagenetic versus epigenetic pyrite is important as these pyrites record different conditions, at different times with various metallogenic and exploration implications. For instance, Large et al. (2011) have proposed that a large part of the Au budget in auriferous systems is sourced from the metamorphic-induced liberation of Au from

sedimentary pyrite. Although this model could be conceivable for certain areas, to our knowledge, it has yet to be demonstrated in the Timmins-Matheson region.

In part, this ongoing research aims to (1) characterize and classify diagenetic versus epigenetic iron sulphides based on textures and geochemical signatures (trace elements and isotopes), (2) improve our understanding of the factors controlling Au uptake in diagenetic pyrite, and (3) use isotope systems to constrain the source of metals from both ore-related and sedimentary pyrite grains. It should be noted that pyrrhotite nodules also occur in the sedimentary rocks of the Timmins-Matheson region but they only represent a small fraction (in abundance) relative to their pyritic counterpart in the study area and will be addressed in a separate publication.

This contribution provides a summary of the various textures observed in pyrite nodules, presents some of the key geochemical attributes of nodules and epigenetic textures (e.g. prophyroblasts, granoblasts, idiomorphic overgrowths) based on robust statistical analysis, describes the recently developed methodology and preliminary results from in situ Fe isotope work using the laser ablation-multi-collector-inductively coupled plasma-mass spectrometry (LA-MC-

ICP-MS), and discusses potential implications for exploration.

GEOLOGICAL SETTING

The study area is within the southwestern portion of the Neoarchean Abitibi greenstone belt, which is part of the Superior Province (Fig. 1). It encompasses seven volcano-sedimentary rock assemblages that range in age from 2734 to <2669 Ma, including (from oldest to youngest) the Deloro, Stoughton-Roquemaure, Kidd-Munro, Tisdale, Blake River, Porcupine, and Timiskaming assemblages (e.g. Ayer et al., 2002a,b, 2005; Bateman et al., 2008). The five oldest assemblages represent near continuous volcanism from 2734 to 2695 Ma with sequences consisting predominantly of komatiite and tholeiitic basalt to calc-alkalic mafic to felsic volcanic and volcaniclastic rocks (e.g. Ayer et al., 2002a, 2005; Bateman et al., 2008). Interflow sedimentary and iron formation units are present but represent only a small volume of the total rock package (e.g. Bateman et al., 2008). The Porcupine (<2690 to <2685 Ma) and Timiskaming (<2679 to <2669 Ma) assemblages, on the other hand, represent thick sedimentary packages with lesser volcanic sequences (Bleeker et al., 1999; Ayer et al., 2002b; Bateman et al., 2008). The base of the Porcupine assemblage is marked by polylithic and polygenic volcaniclastic successions and felsic lapilli tuff (i.e. the Krist Formation) that is overlain by and laterally transitions to carbonaceous argillite, mudstone, siltstone, and greywacke (i.e. Hoyle and Beatty formations). The unconformably overlying fluvial, alluvial, to deltaic Timiskaming assemblage consists of polylithic conglomerate at the base (including local sulphidic fragments; Gray and Hutchinson, 2001), overlain by successions of sandstone and siltstone, including greywacke (Born, 1995).

Two salient east-trending structural features, namely the Destor-Porcupine fault zone and the Pipestone fault, have played an integral role in the geological and metallogenic architecture of the Timmins-Matheson Au corridor (Fig. 1; e.g. Dubé et al., 2017). To the north, the Pipestone fault is interpreted to have developed soon after deposition of the Porcupine assemblage, which was thrust- and fold-imbricated with older volcanic rocks (e.g. the Tisdale assemblage) within major southwest-verging thrust slices (Bleeker, 2015). To the south, the Destor-Porcupine fault zone and associated structures record a complex history of basin subsidence and inversion, and north-directed thick-skinned thrusting, which occurred as a result of north-south shortening at <2669 Ma (Bateman et al., 2008; Dubé et al., 2017). The Timiskaming assemblage is exposed within close proximity of the Destor-Porcupine fault zone and the stratigraphic facies change from conglomerate to mudstone to conglomer-ate is likely the expression of the onset, deepening, and filling of a synorogenic basin (Bleeker, 2015). The bulk of the Au deposits are found along these fault zones and their splays (Fig. 1), which likely acted as important pathways to CO_2-rich metamorphic Au-bearing fluids (Bateman et al., 2008; Dubé et al., 2017).

PYRITE NODULES AND CONCRETIONS

Pyrite nodules are spherical to oblate and can range in size from a few millimetres to 5 centimetres in diameter. They are generally concentrically zoned, which is expressed by their textures that can be separated into two main domains: a core and a rim (Fig. 2a,b). The core exhibits two main types of textures: 1) an equigranular, polycrystalline, fined-grained, anhedral to subhedral pyrite (Fig. 2c,d), and 2) a massive pyrite cementing medium- to coarse-grained detrital inclusions ('cementing texture'), which typically include quartz+albitic to potassic feldspar+mica+Fe-Mg-carbonate±apatite±rutile (Fig. 2e,f, 3a). In low-strain areas, inclusions in nodules typically form layers concordant with bedding. The rims display a variety of textures; Figure 2g to p show the most common ones. Pyrite can develop acicular (Fig. 2g,h), tabular or stubby (Fig. 2i,j), braided (Fig. 2k,l), hexagonal/polygonal prisms (Fig. 2m,n), or skeletal (Fig. 2o,p) textures. The skeletal variety forms cross-hatched elongate crystals, commonly with co-existing sphalerite±chalcopyrite. The braided (or anastomosing) texture is defined by a network of inclusion-rich or 'dusty' pyrite that encloses prismatic, inclusion-poor, outward-oriented pyrite crystals (Fig. 2k,l). Whereas Au concentration is typically low in the rim relative to the core (e.g. Jackson et al., 2017; Pilote et al., 2020), the dusty pyrite in the braided texture can be enriched significantly relative to other common rim textures (Jackson et al., 2017).

Centimetre-scaled and irregular-shaped pyrite growths are also common in the sedimentary sequences. These are referred to as concretions and can be distinguished from nodules only by their shape, which is generally elongated and irregular, also zonation is parallel to bedding (S_0) rather than concentric. Concretions are typically formed of massive pyrite cementing coarse material developed in silty or sandy layers (Fig. 2b, 3a; Pilote et al., 2019) with a texture and mineralogy that resembles the cementing texture in some of the cores of the nodules (Fig. 2e,f). The rim of concretions can also develop similar textures to those of the nodules. Gold can reach multi-ppm levels in nodules and concretions (Jackson et al., 2017; Pilote et al., 2019) but it is invisible (as nano-inclusions and/or in solid-solution; Reich et al., 2005; Fougerouse et al., 2016). Where electrum (Ag-Au alloy) or native gold is
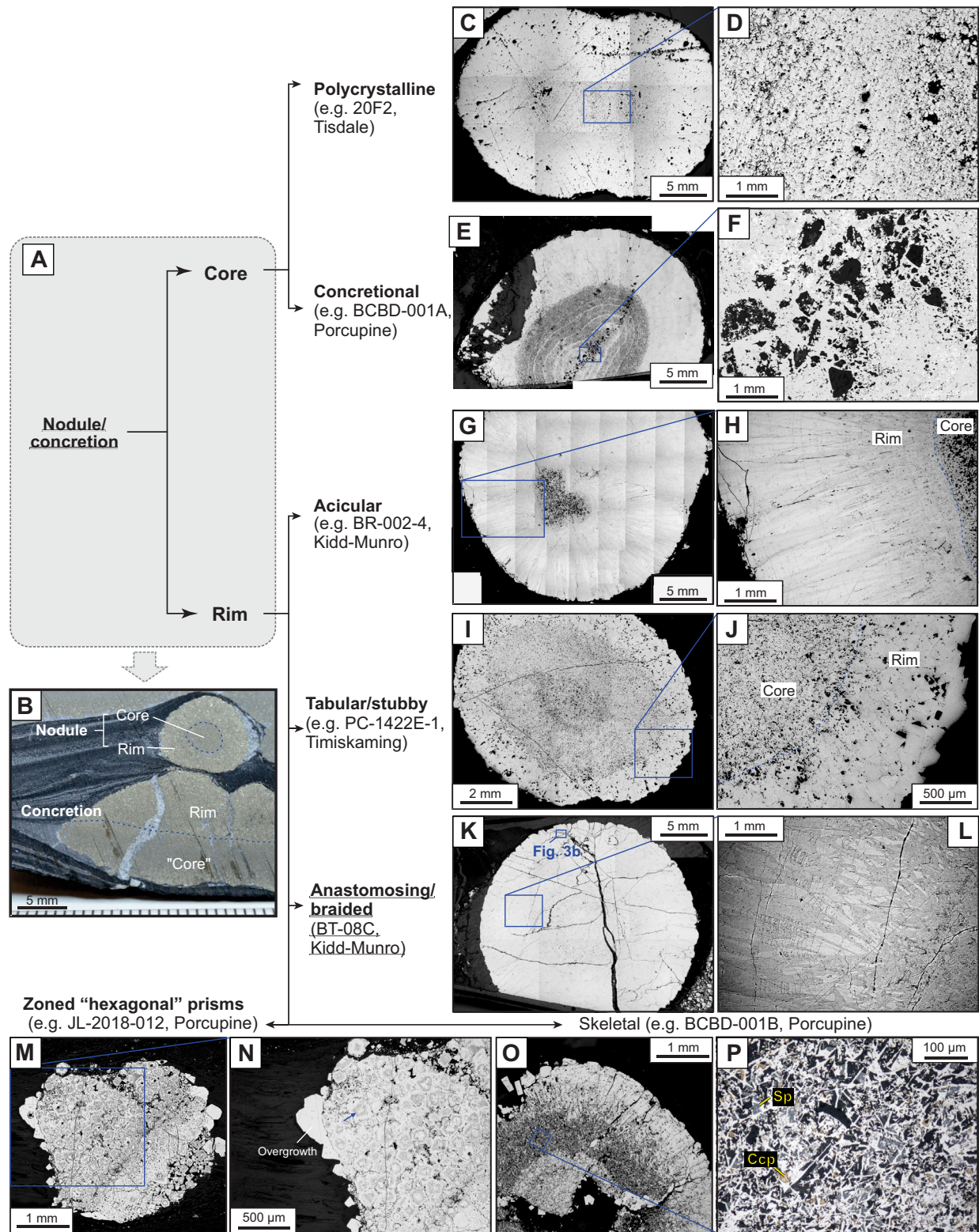
Figure 2. Photos and photomicrographs of representative textures in nodules and concretions from various assemblages of the Timmins-Matheson region. **a, b)** Main domains consisting of a core and rim (sample JL-2019-039, Bradshaw deposit, Kidd-Munro assemblage). **c, d)** Polycrystalline core texture (sample 20F2, Owl Creek deposit, Tisdale assemblage). **e, f)** Cementing texture in the core of a nodule composed of coarser detrital grains (sample BCBD-001A, Bell Creek deposit, Porcupine assemblage). **g, h)** Acicular texture pyrite (sample BR-002-4, Bradshaw deposit, Kidd-Munro assemblage). i, **j)** Tabular or stubby texture pyrite (sample PC-1422E-1, Pamour 1 and Hoyle deposit, Timiskaming assemblage). **k, l)** Braided texture composed of inclusion-poor prismatic crystals surrounded by a network of porous pyrite (sample BT-08C, Holloway deposit, Kidd-Munro assemblage). **m, n)** Agglomeration of zoned hexagonal pyrite (sample JL-2018-012, Bell Creek deposit, Porcupine). **o, p)** Skeletal texture with chalcopyrite (Ccp) and sphalerite (Sp) inclusions (sample BCBD-001B, Bell Creek deposit, Porcupine assemblage).
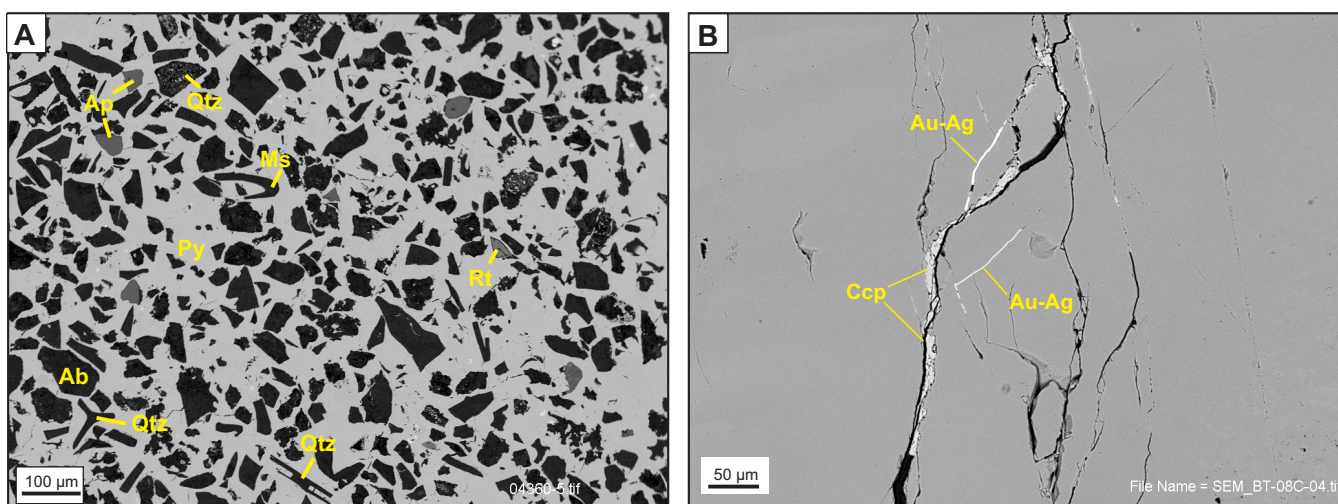
Figure 3. a) Backscattered-electron image of a concretional texture composed of albite (Ab), apatite (Ap), muscovite (Ms), pyrite (Py), quartz (Qtz), and rutile (Rt) (sample 04360, Bell Creek deposit, Tisdale assemblage). **b)** Backscattered-electron image of BT-08C (close-up of Fig. 2k) showing electrum (Au-Ag) and chalcopyrite (Ccp) developed within micro-fractures.

present, it occupies late (micro)fractures that also contain quartz+carbonate±sulphides (Fig. 3b).

METHODS

Trace Element Analysis

More than 1200 laser ablation-inductively coupled plasma-mass spectrometry (LA-ICP-MS) spot analyses were completed of 135 polished thick sections that were made from 122 rock samples from the Timmins-Matheson region. The analyses were performed in static (spot) mode at the Geological Survey of Canada, Ottawa, using an Agilent Technologies 7700 x ICP-MS coupled to a Photon Machines Analyte 193 nm excimer laser ablation system (Cabri and Jackson, 2011). Spot analyses (10–40 μm) were calibrated using USGS doped synthetic basaltic glass standard GSE-1G (Guillong et al., 2005) and doped synthetic pyrrhotite standard Po689 (Co, As, Ag, Sb, and Au; prepared at CANMET). Data reduction was done with the software Glitter™ (Griffin et al., 2008) using "GeoReM preferred values" (http://georem.mpch-mainz.gwdg.de/) for the elemental contents of GSE-1G. Sulphide reference material FeS-1 (LabMaTer, UQAC) was used as an external quality control standard to monitor instrument performance.

To highlight key geochemical features of pyrite in sedimentary rocks of the Timmins-Matheson Au corridor, principal component analysis (PCA) was used to investigate relationships among pyrite composition, textures, and host assemblages (Fig. 4–6). These were computed in the software *R* (R Development Core Team, 2019) after a log-ratio transformation of the data (Filzmoser et al., 2009). Variables included are Mn, Co, Ni, Cu, Zn, As, Se, Mo, Ag, Sb, Au, Tl, Pb, and Bi. Data below the lower detection limit were replaced by dividing the lower detection limit by the square root of

two. Principal components (PC) point in the direction of the main variability of the bulk data. By ranking, the first PC (PC1) explains the maximum variability, the second PC (PC2) explains the second most variability, etc. Simply put, elements that correlate strongly together in a data set will cluster together on a PCA biplot and the further they are from the centre, the more significant they are in defining the structure of the data set. These elements are represented by their PCA loadings, which were rescaled for plotting purposes. The score (of each analysis) is calculated by using a covariance estimator (Filzmoser et al., 2009). Each analysis (or score) represented on the diagram is colour-coded by texture, domain, or host-rock assemblage. Complete data sets will be made available in separate contributions.

Iron Isotope Analysis

Iron isotopic analysis was performed on pyrite nodules from three samples (PC-1422E-1, Pamour Conglomerate in the Timiskaming assemblage; JL-2018-007, Stoughton-Roquemaure assemblage; 20F2, Tisdale assemblage) by laser ablation-multi-collector (MC)-ICP-MS at the Geological Survey of Canada, Ottawa. Two samples were prepared as polished, thick (~100 μm) sections. Analyses were performed in static (spot) analysis mode at intervals along quasi-linear transects from nodule core to rim, immediately adjacent to areas that had undergone prior LA-ICP-MS element mapping. One sample (20F2) was a polished section of a complete pyrite nodule mounted in a 25 mm diameter round epoxy mount. This nodule, which had previously undergone LA-ICP-MS element mapping of the whole nodule, was repolished prior to Fe isotope analysis. Several analyses were also made on narrow pyrite overgrowths on each nodule. Also analyzed were two pyrite
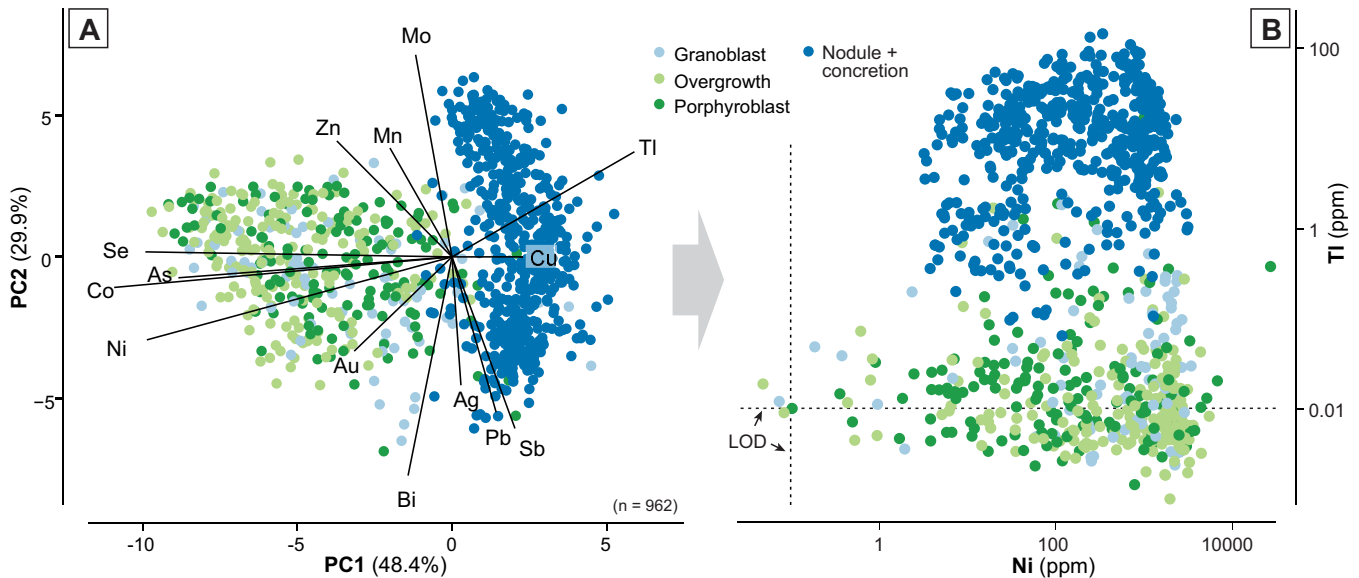
Figure 4. a) Principal component analysis (PCA) biplot of the first two principal components (PC1 and PC2) with their respective variation (in percentage). PCA scores are coloured by type of texture. **b)** Ni (ppm) versus Tl (ppm) of the data displayed in (a). Also shown are lines representing the average lower limits of detection (LOD).

Fe-isotope reference materials that were developed in-house to calibrate analyses and provide quality control: NMC12744 pyrite (Opasatica Lake, Timiskaming County, Quebec, Canada) and Tatlock Quarry pyrite (Lanark County, Ontario, Canada), respectively.

Iron isotopic analysis was performed using a Teledyne Photon Machines Analyte G1 excimer laser ablation system coupled to a Thermo Scientific™ Neptune Plus™ High Resolution MC-ICP-MS. Complete operating conditions are provided in Table 1. All analyses were performed using 43 µm spots and a low laser repetition rate (4 Hz) to minimize down-hole laser-induced isotopic fractionation. A plug of glass wool (~31 mg) in the sample delivery tubing was used to preferentially filter particles (>0.5 µm) too large to be quantitatively volatilized in the ICP, which can result in severe isotopic fractionation (Jackson and Günther, 2003). The Neptune was operated at medium resolution (mass resolving power of ~7700). In this mode, the Fe^+ peaks were resolved from major $^{40}Ar^{14}N^+$, $^{40}Ar^{16}O^+$, $^{40}Ar^{17}O^+/^{40}Ar^{16}O^1H^+$, and $^{40}Ar^{18}O^+$ argide interferences as "flat top" shoulders on the low-mass side of the polyatomic ion peaks (Weyer and Schwieters, 2003). Precise and accurate Fe isotope measurement were then achieved by positioning the centre mass slightly on the low-mass side (~0.001 amu) of the Fe peak (Dauphas et al., 2009). ^{53}Cr and ^{60}Ni were measured to allow correction of ^{54}Cr and ^{58}Ni isobaric interferences on ^{54}Fe and ^{58}Fe, respectively.

MC-ICP-MS signal intensity data were processed offline using an in-house Excel spreadsheet, which performed the following calculations: 1) integration of selected regions of the gas blank and ablation signals,

2) calculation of zero (gas blank) and then isobaric interference-corrected signal intensities and isotope ratios; 3) ±2 sigma outlier rejection; 4) calculation of mean ratios and their uncertainties (within-run precision; 5) application of a mass bias correction using data for pyrite calibration standard NMC12744 analyzed immediately before and after each sample analysis (standard-sample-standard bracketing); and 6) conversion of corrected Fe isotopic ratios and calculated uncertainties (external precision) to $\delta^{57}Fe_{IRMM014}$ and $\delta^{56}Fe_{IRMM014}$ values in per mil (‰), where

$$\delta^{57}Fe_{IRMM014} = ((^{57}Fe/^{54}Fe_{sample})/(^{57}Fe/^{54}Fe_{IRMM014}) - 1) \times 1000$$
and
$$\delta^{56}Fe_{IRMM014} = ((^{56}Fe/^{54}Fe_{sample})/(^{56}Fe/^{54}Fe_{IRMM014}) - 1) \times 1000.$$

Mean $\delta^{57}Fe_{IRMM014}$ and $\delta^{56}Fe_{IRMM014}$ values and external uncertainties for secondary Tatlock Quarry reference pyrite were 0.58 ± 0.23 and 0.39 ± 0.06‰ (2 sd, n = 18 over 3 days), which compare favourably with values of 0.56 ± 0.13 and 0.41 ± 0.09‰, (2 sd, n = 53 over 4 days), respectively, for solution nebulization MC-ICP-MS of digested separates of the same pyrite sample.

RESULTS

Fingerprinting Geochemical Signatures

Comparing nodules and concretions with epigenetic textures

In Figure 4a, calculated PC1 (explains 48.4% of the variance) for the LA-ICP-MS analyses on pyrite nodules/concretions, porphyroblasts, granoblasts, and

Table 1. Laser ablation-multicollector-inductively coupled plasma-mass spectrometry (LA-MC-ICP-MS) operating conditions.

Laser ablation (LA)	
Model	Analyte G1 (Teledyne Photon Machines Inc., USA)
Sample cell	"HelEx" 2-volume cell
Wavelength	193 nm
Pulse duration (FWHM)	4 ns
Repetition rate	4 Hz
Spot diameter	43 µm
Energy density	2.2 J/cm^2
Gas flows:	
Carrier (He) MFC-1 (cell cup)	0.50 Lmin^{-1}
Carrier (He) MFC-2 (cell base)	0.55-0.80 Lmin^{-1}
Make up (Ar)	1.040-1.080 Lmin^{-1}
Signal smoothing	50 mL aerosol mixing tube in sample delivery line
Particle filtering	Plug of glass wool (~31 mg) in sample delivery line
MC-ICP-MS	
Model	Neptune 2 (Thermo-Finnigan, Germany)
Cones	Standard (H) cones
Resolution	Medium resolution (a mass resolving power of ~7700)
Typical signals	8–18 V on ^{56}Fe
Data acquisition parameters	
Data acquisition protocol	Time resolved analysis (0.265 s per reading)
Detectors	Faraday cups equipped with 1011 Ohm resistors
Cup configuration	^{60}Ni (H4), ^{58}Cr (H2), ^{57}Fe (H1), ^{56}Fe (Ax), ^{54}Fe (L2), ^{53}Cr (L4)
Zero	On peak for 60 s prior to ablation
Ablation time	60 s
Calibration and data processing	
Mass bias correction	Standard-sample-standard bracketing
Calibration standard	NMC12744 (QC) in-house pyrite standard
Outlier rejection	± 2 sigma outlier rejection
Quality control standard	Tatlock Quarry (ON) in-house pyrite standard

overgrowths show two main controls: a strongly negative control from Co, Ni, As, and Se, and a strongly positive control from Tl. In PC2 space, which explains 29.9% of the variance, Mn, Zn, Mo, and Tl are positively contributing to the structure of the data set, whereas negative controls are shown for Ag, Sb, Au, Pb, and Bi. When samples (or PCA scores) are plotted in this PC1-PC2 space, a clear separation is shown between the nodules/concretions and the other three textures (Fig. 4a), which is mostly explained by Tl. This separation can also be demonstrated by a simple Ni versus Tl diagram (Fig. 4b) where nodules and concretions show abundances in Tl that are 100 to 10,000 times greater than values observed in epigenetic pyrite, which are generally close to detection limit (i.e. ~0.01 ppm). The data further suggest that elements with positive or negative loadings for PC2 are independent of pyrite texture (Fig. 4a).

Examining element correlations in nodules and concretions

PCA was also done exclusively on data from nodules and concretions to assess internal element correlations and examine features that explain best the structure of the data (Fig. 5; first two PCs only are shown). Figure 5a shows strong positive PC1 loadings for Mn, Zn, Mo, and Tl, and strongly negative loadings for Bi, Pb, Ag, Au, and Sb. In PC2 space, Bi contributed positively, whereas Sb, Au, Cu, Co, and Sb are closely associated with negative PC2 loadings (Fig. 5a). When PCA scores are classified by textural domain, the data from rims and cores largely overlap (Fig. 5a). However, when grouped by lithostratigraphic assemblage, nodules and concretions from the Kidd-Munro assemblage cluster distinctly from the rest of the data, regardless of textural domains (Fig. 5b). The close clustering of different assemblages suggests that intra-grain geochemical variations are less significant than the multivariate compositional differences between pyrite from different host successions. When PCA is done exclusively on cores or rims (Fig. 5c,d), the data also show a separation in PC1-PC2 space for the nodules and concretions from the Kidd-Munro assemblage, best explained by the antithetic contributions of Bi relative to the rest of elements. This is supported by the distinct trace element abundances in the nodules and concretions from the Kidd-Munro assemblage (not shown); for instance, the geometric mean of the Bi content (0.21 and 0.05 ppm Bi in core and rim, respectively) is 10 and 50 times less than for the other assemblages (Pilote et al., unpub. data).

Given the distinct geochemistry that the nodules and concretions have in the Kidd-Munro assemblage, core and rim data were further assessed by individual assemblage (Fig. 6). Only those with the most analyses are shown (i.e. Kidd-Munro, Tisdale, and Porcupine assemblages; Fig. 6a–c). By focusing on individual assemblages, this removes the effect of disparate pyrite compositions that occur between different host-rock assemblages. Nodules and concretions in the Kidd-Munro assemblage have strongly positive loadings for Mo, Zn, and Mn and strongly negative loadings for Sb and Bi in the PC1 space (Fig. 6a). In PC2 space, the strongest positive contributions are explained by Sb, Ag, Co, and Tl, whereas the most negative contributions are from Bi and Ni. In the Tisdale assemblage, Mn, Zn, Mo, and Tl have positive contribution in PC1, whereas they are negative for most elements except Co and Se (Fig. 6b). In PC2 space, Au and Co appear to explain most of the variability, displaying strongly negative contributions (Fig. 6b). As for the Porcupine assemblage, despite the different orientations of the main PCs, variability in the data is comparable to that in the Tisdale assemblage, such as the negative controls
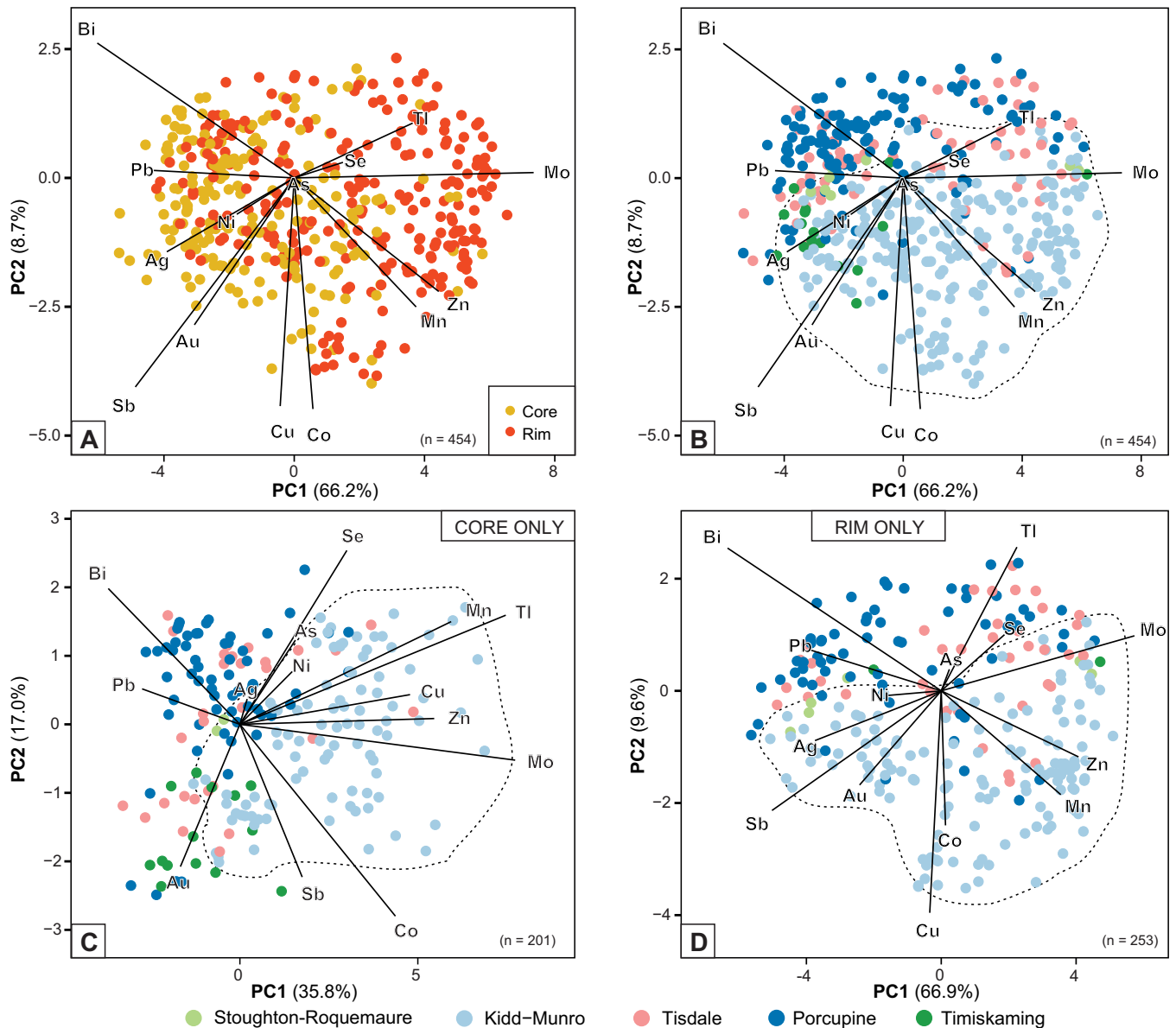
171

Figure 5. Principal component analysis (PCA) biplots of LA-ICP-MS data from nodules and concretions. Only the first two principal components are shown with their respective variation (in percentage). **a)** PCA of data from cores and rims with scores colour-coded by domain. **b)** Same as in (a), but scores are colour-coded by assemblage. **c)** PCA of cores only with scores colour-coded by assemblage. **d)** PCA of data from rims only with scores colour-coded by assemblage.

of Au and Co in PC2 space and the antithetic relationships between Mo and Tl and the rest of the elements in PC1 space (Fig. 6c). In all three assemblages, the variability in the rims are best explained by the behaviour of Mn, Zn, Mo, and Tl, while the cores, although less well defined, are best explained by the covariation of Ni, As, Se, Ag, Sb, Au, Pb, and Bi.

Iron Isotope Results

The three nodules show similar variations but different values in Fe isotope composition (Table 2, Fig. 7). For simplicity, given the linear relationship between $\delta^{56}Fe$ and $\delta^{57}Fe$ (Fig. 7g,h), only values for the former will be described here. The total range in $\delta^{56}Fe$ for all three

samples is $-3.11 \pm 0.09‰$ (2σ) to $+0.97 \pm 0.05‰$ with lighter values in the nodules compared to the overgrowth pyrite grains (Table 2). Across the cores, the Fe isotope values tend to remain relatively constant (within 1‰; Fig. 7d–f). The cores in JL-2018-007 and 20F2 are similar with average values of -2.56 and -2.53‰, respectively, whereas the sample from the Pamour conglomerate (sample PC-1422E-1) shows a significantly heavier core, averaging -0.91‰. Most of the rim in the latter sample shows lighter values than its core, except for two analyses (+0.74 and +0.76‰), which overlap those of the overgrowth pyrite (Fig. 7g). The overgrowth pyrite grains developed around the nodules have significantly heavier values than the rest
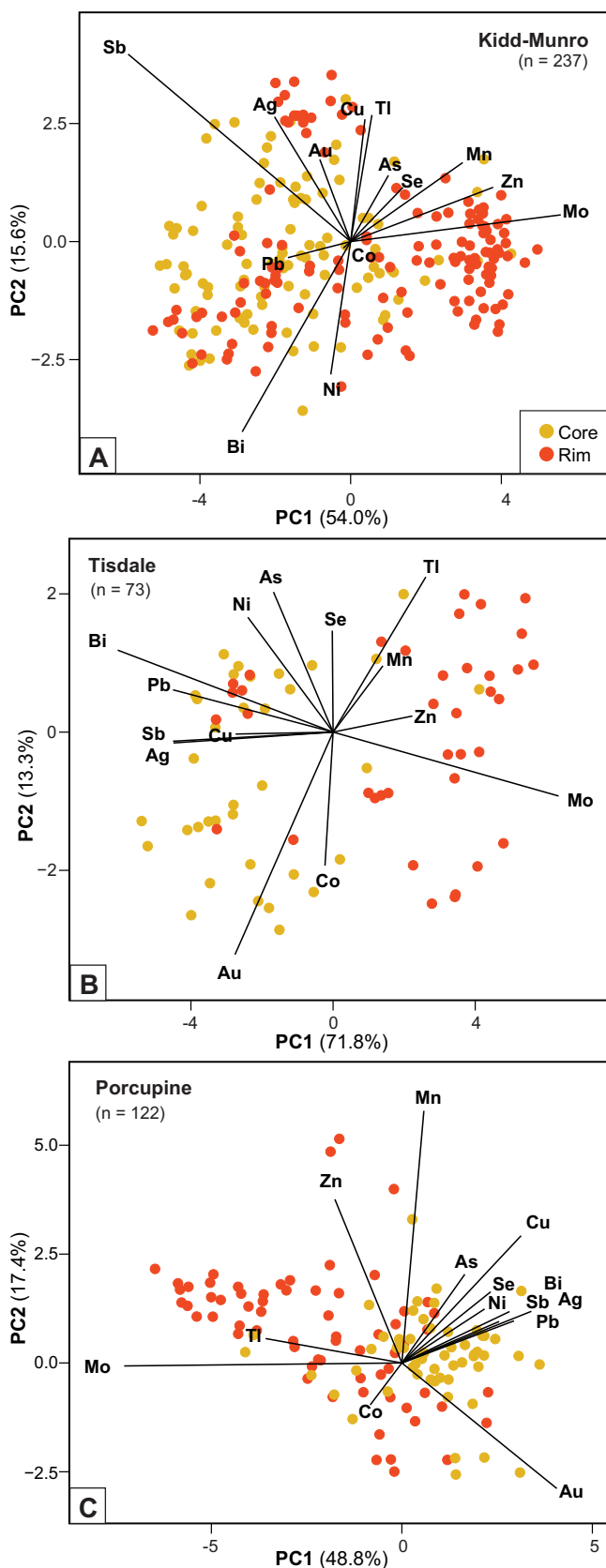
Figure 6. Principal component analysis (PCA) biplots of LA-ICP-MS data from nodules and concretions with scores colour-coded by domain (core or rim). **a)** Data from the Kidd-Munro assemblage. **b)** Data from the Tisdale assemblage. **c)** Data from the Porcupine assemblage.

Table 2. Summary of $\delta^{56}Fe$ values in per mil (‰) notation.

	PC-1422E-1			JL-2018-007			20F2		
	Mean	Min	Max	Mean	Min	Max	Mean	Min	Max
Core	-0.91	-1.97	-0.05	-2.53	-2.67	-2.40	-2.56	-2.72	-2.31
Rim	-1.21	-2.13	0.74	-2.45	-2.89	-1.61	-2.39	-3.11	-1.87
Overgrowth	0.45	-0.04	0.97						
Cataclast				-2.24	-2.68	-1.23			

of the analyzed grains, ranging from -0.04 ± 0.05‰ to +0.97 ± 0.05‰

Iron isotope values in the rim of sample JL-2018-007 overlap those of its core, ranging from -2.89 ± 0.07‰ to -1.61 ± 0.04‰, and display a lighter-to-heavier pattern toward the edge (Fig. 7e). The cataclastic fragments as seen in Figure 7b, show similar values as those of the rim, with a range from -2.68 ± 0.05‰ to -1.23 ± 0.09‰ (Table 2).

The rim of nodule 20F2 shows two distinct trends, which appear to reflect differences in textures. Much like nodule BT-08C (Fig. 2k,l), the rim of sample 20F2 is characterized by a braided network of dusty pyrite ("A" in Fig. 7c) enclosing massive, inclusion-poor, euhedral crystals ("B" in Fig. 7c). The progressive increase in $\delta^{56}Fe$ (and $\delta^{57}Fe$) values from core to rim of the dusty pyrite correlate with the continuous textural transition observed in thin section (Fig. 7f). The clean euhedral crystals, however, show a distinctively lighter and flat pattern (Fig. 7f), which ranges between -2.6 and -2.4‰, as opposed to a range from -2.2 to -1.9‰ for the dusty pyrite.

DISCUSSION

Detailed field and petrographic observations reveal that despite textural complexities among argillite-hosted nodules and concretions (Fig. 2), commonalities exist across variably aged volcanic and sedimentary assemblages in the Timmins-Matheson Au corridor, regardless of the setting of the sediment deposition (e.g. volcanic interflows, deep-water basin-related), deformation, metamorphism, and/or alteration. Samples collected within 10 m of shear-hosted orogenic Au mineralization (e.g. Bradshaw, Bell Creek) showed no systematic textural differences to those sampled from 'greenfield' exploration drill cores (>10 km from any known ore-grade mineralization). Nodules that developed in the argillic sequences associated with the LaRonde Penna VMS deposit (Blake River Group; Mercier-Langevin et al., 2007) also display the same transition from a polycrystalline core to a crystalline rim (Pilote et al., 2020).

Multivariate statistical analysis of >1200 LA-ICP-MS spot analyses show that nodules and concretions from the Timmins-Matheson Au corridor have very distinct geochemical signatures compared to those with epigenetic textures (granoblastic, porphyroblastic, and
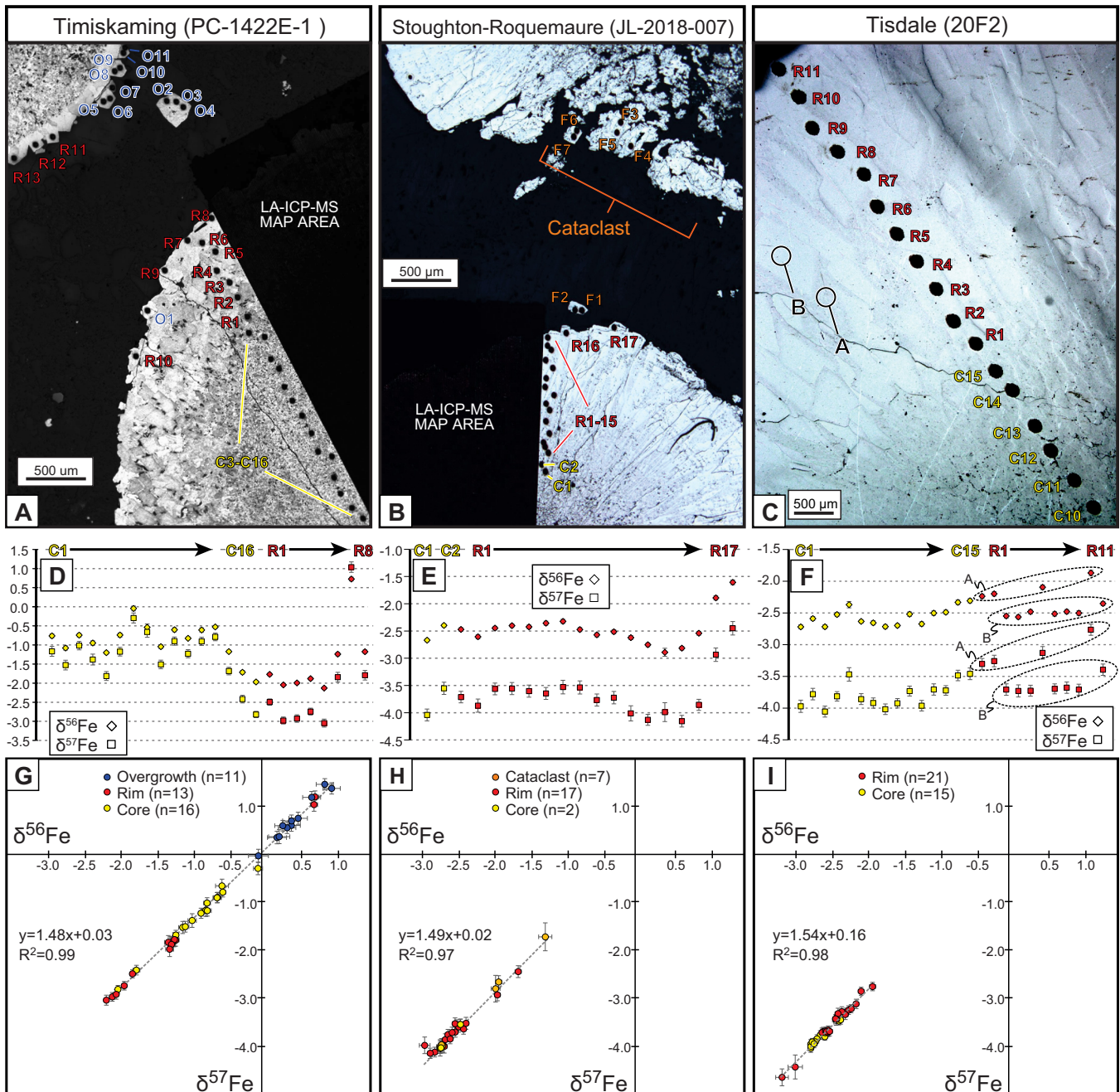
173

Figure 7. a to c) Photomicrographs (reflected light) of nodules with locations of Fe isotope analysis by LA-MC-ICP-MS. **d to f)** δ⁵⁶Fe and δ⁵⁷Fe values for transects across the nodules in a to c. **g to i)** Complete Fe isotope analyses represented on a δ⁵⁶Fe versus δ⁵⁷Fe biplot. The regression reflects the mass-dependent fractionation of the isotopes. Error bars represent ±2 standard deviations of the mean.

overgrowths in grains showing multiple growth zones and hosted in argillite, basaltic/ultramafic flows, mafic dykes, or quartz-carbonate veins). This is reflected mainly by the abundance of Tl in pyrite as seen in Figure 4b.

Geometric means of trace element abundances, including Au, in the nodules varies greatly from core to rim but also from the core of one nodule to another (Pilote et al., 2019). Despite this, systematic element patterns—shown here by PCA within the core and

rim—suggest that, on the scale of a nodule, the evolving physical (e.g. permeability) and/or chemical (e.g. supersaturation of reactants, i.e., reduced Fe and S, redox) conditions controlling element uptake during crystal growth must be largely comparable, regardless of the host-rock composition. It is currently understood that the concentric zoning of a nodule reflects growth in closed or highly isolated conditions (Gregory et al., 2019) in a stagnant or gently advective hydrodynamic regime (Rickard, 2012) and that the textural transition
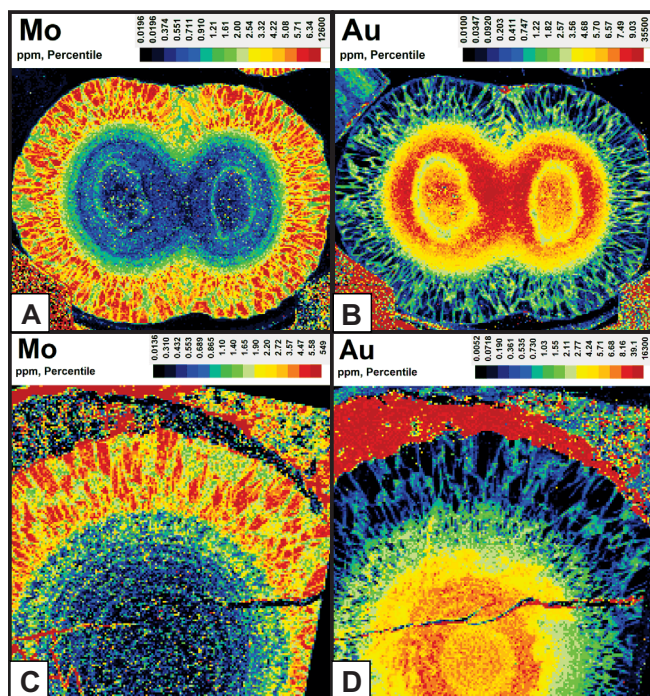
Figure 8. LA-ICP-MS element maps of nodules. **a)** Mo and **b)** Au in sample 20F2 (Owl Creek deposit, Tisdale assemblage; *see* Fig. 2c for photomicrograph). **c)** Mo and **d)** Au in sample BT-08C (Holloway deposit, Kidd-Munro assemblage; *see* Fig. 2k for photomicrograph). Note the distribution of Au in both samples and the high Au values along the fracture in BT-08C. The element maps use a percentile colour-scaling function.

from a fine polycrystalline core to a prismatic rim is the result of a decrease in the state of supersaturation (Murowchick and Barnes, 1987; Rickard, 2012; Hu et al., 2019). The cores are generally enriched in Ni, As, Se, Ag, Sb, Au, Pb, and Bi relative to the rims, which is validated by detailed LA-ICP-MS compositional mapping of more than 20 nodules from the Timmins region, which will be the subject of a separate contribution (preliminary results shown in Jackson et al., 2017 and Pilote et al., 2019). The rims are commonly strongly enriched in Mo, two examples of which are shown in Figure 8. This enrichment correlates with the development of prismatic pyrite and could be related to the change in pyrite crystallinity. Alternatively, the sudden enrichment in Mo could be related to a change in pH and/or redox in the sediment pore fluids, optimizing MoS_4^{2-} adsorption during crystal growth (Bostick et al., 2003). Because Mo and Au concentrations are antithetic in these two map examples on PCA biplots (Fig. 4), the process(es) controlling enrichment of accessory elements have important implications for Au fertility. Factors controlling the variability of Au (and other trace elements) from one nodule/concretion core to another are not fully understood but preliminary conclusions from this research activity suggest that Au abundance (multi-ppb versus -ppm levels) in cores

could be predominantly linked to Au availability in the matrix sediments (Pilote et al., work in progress).

The interpretation of Fe-isotope signatures in Archean shale remains equivocal (e.g. Rouxel et al., 2005, 2006; Dauphas et al., 2017) because the processes giving rise to isotopic fractionation are incompletely understood. It is however recognized that the Fe isotopic ratio is largely regulated by (abiotic or biotic) redox reactions (Rouxel et al., 2005; Nishizawa et al., 2010; Yoshiya et al., 2012). The δ^{56}Fe range observed in the three pyrite nodules from Timmins overlaps with the values of the diagenetic pyrite grains in Neoarchean shale reported elsewhere (-3.5 to +0.5‰; *see* compilation in Dauphas et al., 2017). Moreover, many of the isotopically light pyrite values (<-2.5‰) observed in the Timmins samples (Fig. 7) are thought to only occur in diagenetic pyrite from pre-2.5 Ga black shale as a result of depletion of isotopically heavy Fe associated with partial Fe(II) oxidation and precipitation of Fe oxides from a globally anoxic, Fe-rich Neoarchean ocean (Dauphas et al., 2017). By contrast, sedimentary pyrite in post-2.5 Ga sedimentary sequences and pyrite of hydrothermal origin show smaller Fe isotopic ranges, with respective mean values that are close to modern oceanic values (i.e. dissolved δ^{56}Fe of ~0 to +0.5‰: Radic et al., 2011) and igneous rocks and hydrothermal sources (-0.8 to +0.2‰) (Dauphas et al., 2017).

At the intra-grain level, a study by Marin-Carbonne et al. (2014) on shale-hosted pyrite nodules from the ca. 2.7 Ga low-grade metamorphic rocks of the Bubi greenstone belt, Zimbabwe, reported in situ δ^{56}Fe values ranging from -2.1 to 0.7‰; a core displaying lighter values than its rim, correlating with an outward depletion in Ni and enrichment in Co. These values and patterns are strikingly similar to the three nodules from the Timmins region. Marin-Carbonne et al. (2014) interpret this relatively large negative excursion as the product of multiple Fe sources (metastable iron sulphides formed in seawater and the sediment) during complex early diagenetic processes.

EXPLORATION IMPLICATIONS

Careful examination is strongly encouraged before interpreting the genesis of pyrite in sedimentary rocks, particularly those in high-strain zones and/or medium- to high-grade metamorphic belts. The authigenic nodules and concretions described here show zoning and textural, chemical, and isotopic characteristics similar to those resulting from diagenetic processes reported elsewhere (e.g. Bonnell and Anderson, 1987; Rickard, 2012; Jeans et al., 2016; Gregory et al., 2019). However, 'nodular' pyrite composed entirely of medium- to coarse-grained, porous, idiomorphic pyrite and quartz enclosing visible Au grains near mineralized

175

zones have also been reported in carbonaceous argillite in the Timmins region. For example, Jonasson et al. (1999) described examples of such textures from the Owl Creek Au deposit and interpreted them to be the product of epigenetic hydrothermal processes (*see* Fig. 9e,f in Jonasson et al., 1999). Similar pyrite textures investigated in this study yield low Tl values (≤0.1 ppm), much like the other epigenetic textures studied in the Timmins region. Therefore, although interpreted to be epigenetic, their rounded nature could potentially be mistaken as diagenetic in the field.

The composition of diagenetic pyrite nodule cores can vary greatly and can contain up to >10 ppm Au; however, Au is refractory (or invisible), which is not optimal for metallurgical recovery. On a broader scale, if the amount of Au in diagenetic pyrite predisposes a region (among many other parameters; e.g. Hronsky et al., 2012) to be fertile and conducive for hosting orogenic-type mineralization as proposed by Large et al. (2011), then the spatial pairing that exists between the Au-enriched pyrite nodules and the Au endowment of the Timmins-Matheson Au corridor may be related. However, research on orogenic Au deposits has shown that many more elements are at play in forming world-class Au districts and equating sulphidic argillite and Au may be an oversimplification of a multi-parameter process. It is premature at this point to draw any conclusion about the potential role of the pyrite nodules (and other diagenetic pyrite) on the Au budget in a giant district such as the auriferous Timmins-Porcupine camp.

ONGOING WORK

Whereas significant progress has been made, many questions remain unanswered and important hypotheses remain untested in the Timmins-Matheson Au corridor. Ongoing work includes interrogation of multiple isotope systems (Fe, Pb, and S) by LA-MC-ICP-MS and ion microprobe on diagenetic and epigenetic iron sulphides, both proximal and distal to mineralization. Approximately 200 of the spots targeted for isotope analysis have also been analyzed by LA-ICP-MS for trace element abundances. A total of 31 LA-ICP-MS compositional maps have been generated (29 from the Timmins region and two from the LaRonde deposit; Pilote et al., 2020). The millions of data points derived from these maps have been classified via robust multi-variate statistics and clustering methods to quantitatively define intra-grain pyrite generations and compare them within and between rock assemblages. Whole-rock geochemistry of the sedimentary host to the nodules and concretions is complete and the combination of in situ and whole-rock data will provide an opportunity to examine possible factors controlling and trace element uptake in pyrite by using, for example,

various redox, provenance, and hydrothermal proxies. This multi-technique approach, combined with detailed field work, will provide, in part, a way to minimize the uncertainties related to the interpretation of the possible Au source(s).

REFERENCES

Ayer, J., Amelin, Y., Corfu, F., Kamo, S., Ketchum, J., Kwok, K., and Trowell, N., 2002a. Evolution of the southern Abitibi greenstone belt based on U-Pb geochronology: Autochthonous volcanic construction followed by plutonism, regional deformation and sedimentation; Precambrian Research, v. 115, p. 63–95.

Ayer, J.A., Ketchum, J.W.F., and Trowell, N.F., 2002b. New geochronological and neodymium isotopic results from the Abitibi greenstone belt, with emphasis on the timing and the tectonic implications of Neoarchean sedimentation and volcanism; Ontario Geological Survey, Open File Report 6100, p. 5-1–5-16.

Ayer, J.A., Thurston, P.C., Bateman, R., Dubé, B., Gibson, H.L., Hamilton, M.A., Hathway, B., Hocker, S.M., Houlé, M.G., Hudak, G., Ispolatov, V.O., Lafrance, B., Lesher, C.M., MacDonald, P.J., Péloquin, A.S., Piercey, S.J., Reed, L.E., and Thompson, P.H., 2005. Overview of results from the Greenstone Architecture Project: Discover Abitibi Initiative; Ontario Geological Survey. Open File Report 6154, 146 p.

Barnicoat, A.C., Henderson, I.H.C., Knipe, R.J., Yardley, B.W.D., Napier, R.W., Fox, N.P.C., Kenyon, A.K., Muntingh, D.J., Strydom, D., Winkler, K.S., Lawrence, S.R., and Cornford, C., 1997. Hydrothermal gold mineralisation in the Witwatersrand Basin; Nature, v. 386, p. 820–824.

Bateman, R., Ayer, J.A., and Dubé, B., 2008. The Timmins-Porcupine gold camp, Ontario: Anatomy of an Archean greenstone belt and ontogeny of gold mineralization; Economic Geology, v. 103, p. 1285–1308.

Bleeker, W., 2015. Synorogenic gold mineralization in granite-greenstone terranes: The deep connection between extension, major faults, synorogenic clastic basins, magmatism, thrust inversion, and long-term preservation; *in* Targeted Geoscience Initiative 4: Contributions to the Understanding of Precambrian

Lode Gold Deposits and Implications for Exploration, (ed.) B. Dubé, and P. Mercier-Langevin; Geological Survey of Canada, Open File 7852, p. 25–47.

Bleeker, W., Parrish, R.R., and Sager-Kinsman, A., 1999. High-precision U-Pb geochronology of the Late Archean Kidd Creek deposit and Kidd volcanic complex; *in* The Giant Kidd Creek Volcanogenic Massive Sulfide Deposit, western Abitibi Subprovince, Canada, (ed.) M.D. Hannington and C.T. Barrie; Society of Economic Geologists, Monograph 10, p. 43–70.

Bonnell, L. and Anderson, T.F., 1987. Sulfur isotopic variations in nodular and disseminated pyrite: hole 603B; *in* Initial Reports of the Deep Sea Drilling Project, (ed.) J.E. van Hinte et al.; U.S. Government Printing Office, Washington, p. 1257–1262.

Born, P., 1995. A sedimentary basin analysis of the Abitibi greenstone belt in the Timmins area, northern Ontario, Canada; Ph.D. thesis, Carleton University, Ottawa, Ontario, 489 p.

Bostick, B.C., Fendorf, S., and Helz, G.R., 2003. Differential adsorption of molybdate and tetrathiomolybdate on pyrite (FeS_2); Environmental Science and Technology, v. 37, p. 285–291.

Cabri, L. and Jackson, S., 2011. New developments in characterization of sulfide refractory Au ores; World Gold 2011, 50th Conference of Metallurgists, MetSoc, Montreal, Quebec, p. 51–62.

Dauphas, N., Pourmand, A., and Teng, F.-Z., 2009. Routine isotopic analysis of iron by HR-MC-ICPMS: How precise and how accurate?; Chemical Geology, v. 267, p. 175–184.

Dauphas, N., John, S.G., and Rouxel, O., 2017. Iron isotope systematics; Reviews in Mineralogy and Geochemistry, v. 82, p. 415–510.

Dubé, B., Mercier-Langevin, P., Ayer, J., Atkinson, B., and Monecke, T., 2017. Orogenic greenstone-hosted quartz-carbonate gold deposits of the Timmins-Porcupine camp; *in* Archean Base and Precious Metal Deposits, southern Abitibi Greenstone Belt, Canada, (ed.) T. Monecke, P. Mercier-Langevin, and B. Dubé; Reviews in Economic Geology, v. 19, p. 51–79.

Filzmoser, P., Hron, K., and Reimann, C., 2009. Principal component analysis for compositional data with outliers; Environmetrics, v. 20, p. 621–632.

Fougerouse, D., Reddy, S.M., Saxey, D.W., Rickard, W.D.A., van Riessen, A., and Micklethwaite, S., 2016. Nanoscale gold clusters in arsenopyrite controlled by growth rate not concentration: Evidence from atom microscopy; American Mineralogist, v. 101, p. 1916–1919.

Gray, M.D. and Hutchinson, R.W., 2001. New evidence for multiple periods of gold emplacement in the Porcupine mining district, Timmins area, Ontario, Canada; Economic Geology, v. 96, p. 453–475.

Gregory, D., Mukherjee, I., Olson, S.L., Large, R.R., Danyushevsky, L.V., Stepanov, A.S., Avila, J.N., Cliff, J., Ireland, T.R., Raiswell, R., Olin, P.H., Maslennikov, V.V., and Lyons, T.W., 2019. The formation mechanisms of sedimentary pyrite nodules determined by trace element and sulfur isotope microanalysis; Geochimica et Cosmochimica Acta, v. 259, p. 53–68.

Griffin, W., Powell, W., Pearson, N., and O'Reilly, S., 2008. GLITTER: Data reduction software for laser ablation ICP-MS; *in* Laser Ablation ICP-MS in the Earth Sciences; Current Practices and Outstanding Issues, (ed.) P.J. Sylvester; Mineralogical Association of Canada, Short Course 40, p. 308–311.

Guillong, M., Hametner, K., Reusser, E., Wilson, S.A., and Günther, D., 2005. Preliminary characterisation of new glass reference materials (GSA-1G, GSC-1G, GSD-1G and GSE-1G) by laser ablation-inductively coupled plasma-mass spectrometry using 193 nm, 213 nm and 266 nm wavelengths; Geostandards and Geoanalytical Research, v. 29, p. 315–331.

Guy, B.M., Beukes, N.J., and Gutzmer, J., 2010. Paleo-environmental controls of pyrite from non-conglomeratic sedimentary rocks of the Mesoarchean Witwatersrand Supergroup, South Africa; South African Journal of Geology, v. 113, p. 195–228.

Guy, B.M., Ono, S., Gutzmer, J., Lin, Y., and Beukes, N.J., 2014. Sulfur sources of sedimentary "buckshot" pyrite in the auriferous conglomerates of the Mesoarchean Witwatersrand and Ventersdorp Supergroups, Kaapvaal Craton, South Africa; Mineralium Deposita, v. 49, p. 751–775.

Hannington, M.D., Bleeker, W., and Kjarsgaard, I., 1999. Sulfide mineralogy, geochemistry, and ore genesis of the Kidd Creek deposit: Part I. North, Central, and South Orebodies; *in* The Giant Kidd Creek Volcanogenic Massive Sulfide Deposit, western Abitibi Subprovince, Canada, (ed.) M.D. Hannington and C.T. Barrie; Society of Economic Geologists, Monograph 10, p. 163–224.

Hannington, M.D., Coombs, A., van Hees, G., Duff, S., and Campos-Alvarez, N., 2012. Regional lithogeochemical study of the Kidd–Munro MEGATEM® survey areas, Timmins–Kirkland Lake, northern Ontario: Discover Abitibi Initiative; Ontario Geological Survey, Miscellaneous Release Data 291, 209 p.

Houlé, M.G., Lesher, C.M., Préfontaine, S., Ayer, J.A., Berger, B.R., Taranovic, V., Davis, P.C., and Atkinson, B. 2010. Stratigraphy and physical volcanology of komatiites and associated Ni-Cu-(PGE) mineralization in the western Abitibi greenstone belt, Timmins area, Ontario: a field trip for the 11th International Platinum Symposium; Ontario Geological Survey, Open File Report 6255, 99 p.

Hronsky, J.M.A., Groves, D.I., Loucks, R.R., and Begg, G.C., 2012. A unified model for gold mineralisation in accretionary orogens and implications for regional-scale exploration targeting methods; Mineralium Deposita, v. 47, p. 339–358.

Hu, S., Barnes, S.J., Glenn, A.M., Pagès, A., Parr, J., MacRae, C., and Binns, R., 2019. Growth history of sphalerite in a modern sea floor hydrothermal chimney revealed by electron backscattered diffraction; Economic Geology, v. 114, p. 165–176.

Jackson, S.E. and Günther, D., 2003. The nature and sources of laser induced isotopic fractionation in laser ablation-multi-collector-inductively coupled plasma-mass spectrometry; Journal of Analytical Atomic Spectrometry, v. 18, p. 205–212.

Jackson, S.E., Dubé, B., Mercier-Langevin, P., and Rhys, D., 2017. Fingerprinting ore processes in auriferous systems; *in* Targeted Geoscience Initiative – 2016 Report of Activities, (ed.) N. Rogers; Geological Survey of Canada, Open File 8199, p. 29–32.

Jeans, C.V., Turchyn, A.V., and Hu, X., 2016. Sulfur isotope patterns of iron sulfide and barite nodules in the Upper Cretaceous Chalk of England and their regional significance in the origin of coloured chalks; Acta Geologica Polonica, v. 66, p. 227–256.

Jonasson, I.R., Kingston, D.M., Watkinson, D.H., and Elliot, S.R., 1999. Role of pyrite in the formation and localization of gold mineralization at the Owl Creek mine, Timmins, Ontario; *in* The Giant Kidd Creek Volcanogenic Massive Sulfide Deposit, western Abitibi Subprovince, Canada, (ed.) M.D. Hannington and C.T. Barrie; Society of Economic Geologists, Monograph 10, p. 627–660.

Large, R.R., Bull, S.W., and Maslennikov, V.V., 2011. A carbonaceous sedimentary source rock model for Carlin-type and orogenic gold deposits; Economic Geology, v. 106, p. 331–358.

Marin-Carbonne, J., Rollion-Bard, C., Bekker, A., Rouxel, O., Agangi, A., Cavalazzi, B., Wohlgemuth-Ueberwasser, C.C., Hofmann, A., and McKeegan, K.D., 2014. Coupled Fe and S

isotope variations in pyrite nodules from Archean shale; Earth and Planetary Science Letters, v. 392, p. 67–79.

Mercier-Langevin, P., Dubé, B., Hannington, M.D., Davis, D.W., Lafrance, B., and Gosselin, G., 2007. The LaRonde Penna Au-rich volcanogenic massive sulfide deposit, Abitibi greenstone belt, Quebec: Part I. Geology and geochronology; Economic Geology, v. 102, p. 585–609.

Murowchick, J.B. and Barnes, H.L., 1987. Effects of temperature and degree of supersaturation on pyrite morphology; American Mineralogist, v. 72, p. 1241–1250.

Nishizawa M., Yamamoto, H., Ueno, Y., Tsuruoka, S., Shibuya, T., Sawaki, Y., Yamamoto, S., Kon, Y., Kitajima, K., and Komiya, T., 2010. Grain-scale iron isotopic distribution of pyrite from Precambrian shallow marine carbonate revealed by a femtosecond laser ablation multicollector ICP-MS technique: possible proxy for the redox state of ancient seawater; Geochimica et Cosmochimica Acta, v. 74, p. 2760–2778.

Phillips, G.N. and Law, J.D., 2000. Witwatersrand gold fields: geology, genesis, and exploration; *in* Gold in 2000, (ed.) S.G. Hagemann and P.E. Brown; Reviews in Economic Geology, v. 13, p. 439–500.

Pilote, J.-L., Jackson, S.E., Mercier-Langevin, P., Dubé, B., and Rhys, D., 2019. Characteristics of diagenetic and epigenetic sulphides in deformed and metamorphosed Archean carbonaceous metasedimentary rocks of the Timmins-Matheson corridor: establishing a framework for fingerprinting ore-forming processes in shear zone-hosted orogenic gold systems; *in* Targeted Geoscience Initiative: 2018 report of activities, (ed.) N. Rogers; Geological Survey of Canada, Open File 8549, p. 33–41.

Pilote, J.-L., Mercier-Langevin, P., Jackson, S.E., Dubé, B., Yang, Z., Lawley, C.J.M., Petts, D.C., Layne, G., and Piercey, S.J., 2020. Interrogating the composition and genesis of argillite-hosted pyrite nodules at the LaRonde Penna Au-rich volcanogenic massive sulphide deposit, Abitibi, Quebec: Insights into metallogenic implications; *in* Targeted Geoscience Initiative 5: Contributions to the Understanding of Canadian Gold Systems, (ed.) P. Mercier-Langevin, C.J.M. Lawley, and S. Castonguay; Geological Survey of Canada, Open File 8712, p. 75–91. doi10.4095/323666

R Development Core Team, 2019. R: A language and environment for statistical computing: R Foundation for Statistical Computing, Vienna, Austria. <https://www.R-project.org/>

Radic, A., Lacan, F., and Murray, J.W., 2011. Iron isotopes in the seawater of the equatorial Pacific Ocean: New constraints for the oceanic iron cycle; Earth and Planetary Science Letters, v. 306, p. 1–10.

Reich, M., Kesler, S.E., Utsunomiya, S., Palenik, C.S., Chryssoulis, S.L., and Ewing, R.C., 2005. Solubility of gold in arsenian pyrite; Geochimica et Cosmochimica Acta, v. 69, p. 2781–2796.

Rickard, D.T., 2012. Sulfidic sediments and sedimentary rocks: Developments in sedimentology; Amsterdam, Elsevier, 816 p.

Rouxel, O.J., Bekker, A., and Edwards, K.J., 2005. Iron isotope constraints on the Archean and Paleoproterozoic ocean redox state; Science, v. 307, p. 1088–1091.

Rouxel, O.J., Bekker, A., and Edwards, K.J., 2006. Response to comment on "Iron isotope constraints on the Archean and Paleoproterozoic ocean redox state"; Science, v. 311, p. 177.

Weyer, S. and Schwieter, J.B., 2003. High precision Fe isotope measurements with high mass resolution MC-ICPMS; International Journal of Mass Spectrometry, v. 226, p. 355–368.

Yoshiya, K., Nishizawa, M., Sawaki, Y., Ueno, Y., Komiya, T., Yamada, K., Yoshida, N., Hirata, T., Wada, H., and Maruyama, S., 2012. In situ iron isotope analyses of pyrite and organic carbon isotope ratios in the Fortescue Group: Metabolic variations of a Late Archean ecosystem; Precambrian Research, v. 212, p. 169–193.